Cross-Scale Modeling and Simulation of Coal Pyrolysis to Acetylene in Hydrogen Plasma Reactors

Binhang Yan, Yi Cheng, and Yong Jin
Dept. of Chemical Engineering, Beijing Key Laboratory of Green Chemical Reaction Engineering and Technology, Tsinghua University, Beijing 100084, P.R. China

DOI 10.1002/aic.13984
Published online January 7, 2013 in Wiley Online Library (wileyonlinelibrary.com)

Coal pyrolysis to acetylene in hydrogen plasma is carried out under ultrahigh temperature and milliseconds residence time. To better understand the complex gas-particle reaction behavior, a comprehensive computational fluid dynamics with discrete phase model has been established, with special consideration of the particle-scale physics such as the heat conduction inside particle. The improved chemical percolation devolatilization model that incorporates the tar cracking reactions is adopted. The model predictions are in good agreement with the performances of two pilot-plant reactors. The simulations reveal the detailed unmeasurable information of gas phase and particle-scale behaviors, then point out the facts that coal devolatilization almost finishes in the first 100 mm of the reaction chamber and the optimal particle diameter is suggested to be 20–50 μm. The different reactor performances during the scale-up from 2- to 5-MW unit are analyzed based on the detailed simulation results in combination with the operational experience. © 2013 American Institute of Chemical Engineers *AIChE J*, 59: 2119–2133, 2013

Keywords: coal pyrolysis, acetylene, thermal plasma, computational fluid dynamics, reacting flow simulation

Introduction

Acetylene (C_2H_2) is an important chemical material and widely used for the manufacture of a number of large volume chemicals such as vinyl chloride (for producing PVC), vinyl acetate, acrylonitrile, acetaldehyde, and so on. Nowadays, acetylene is mainly manufactured by the partial oxidation of methane, or appears as a side product in the ethylene stream from cracking of hydrocarbons in the world. However, for the limited resource of natural gas and crude oil in China, the production of C_2H_2 is still dominated by calcium carbide (CaC_2) method, occupying about 90% of the total C_2H_2 production. According to the operational experience in Xinjiang Tianye (Group) Co., the largest PVC producer in China producing 1 ton C_2H_2 would consume 1 ton standard coal, 2 tons coke, 7 tons lime, 3 tons water, 12,000 kWh, and emit 27 tons CO_2, 3.5 tons CaC_2 residue, 14–18 tons waste water, and acid gases such as H_2S and SO_2[1]. According to statistics by the chlor-alkali association of China, the production capacity of PVC in 2010 has reached about 21 million tons per year, where more than 80% adopts the acetylene route, occupying 30% of the total in the world. Cleaner production of C_2H_2 has, therefore, become the paramount goal to implement high-efficient, energy saving, and emission reduction process to produce PVC.

Coal pyrolysis in hydrogen plasma provides a direct and clean means for producing acetylene from coal resources. This process is carried out in a multiphase reactor, which accommodates the high-temperature reactions of coal pyrolysis in milliseconds. This clean coal conversion technique for producing acetylene was discovered by Bond et al.[2] using a plasma jet in the 1960 s. Since then, many researchers have investigated this coal pyrolysis process worldwide. Bond et al.,[2,3] Nicholson and Littlewood[4] summarized the influence of plasma atmosphere on the reactions of coal and acetylene yield; Bond et al.,[3] Grave et al.,[5] Gannon et al.,[6] and Chakravartty et al.[7] investigated the effects of coal feed rate and particle size on coal conversion to acetylene; Bond et al.,[3] Chakravartty et al.,[7] and Bittner et al.[8] studied the relationship between coal properties and acetylene yield. Besides, several attempts had been made to optimize the pyrolysis process during the last century.[9–11] It is worth mentioning that the first ever reported pilot-plant production was the AVCO Arc-Coal process using a prototype of 1-MW plasma reactor in the early 1980 s.[12,13] The specific energy requirement achieved in the tests is 10.5 kWh/kg·C_2H_2 using the water quench and 6.1 kWh/kg·(C_2H_2 + C_2H_4) while using the propane quench. Therefore, Patrick and Gannon[12] had pointed out that "… the arc-coal process is a coal based process which can economically compete with oil based process today."

Since 2002, two sets of the largest pilot-plant plasma reactor facilities in the world (i.e., 2- and 5-MW) have been successfully built in China.[14] The best operation results show the bright future of this advanced coal conversion process: the total energy cost saves about 25%, carbon dioxide emissions reduces about 50%, water consumption saves about 60%, and the materials saving in terms of the coal is about 40% in comparison with the CaC_2 method. For the inherent challenge to develop such a process under high temperature

Correspondence concerning this article should be addressed to Y. Cheng at yicheng@tsinghua.edu.cn.

© 2013 American Institute of Chemical Engineers

(e.g., ~3000 K) and milliseconds contact time, reactor scale-up is actually very difficult for lacking the fundamental knowledge and relevant experience. Besides, direct measurement inside the reactor in such a severe environment can be hardly implemented. Therefore, neither physical nor chemical information can be obtained directly inside the reactor. Therefore, the establishment of a comprehensive computational fluid dynamics (CFD) model incorporating the mechanism of heat transfer, coal devolatilization, and volatile reactions has an important significance for optimizing the operating conditions and guiding the reactor scale-up.

Devolatilization of coal, which is believed to be the first chemical conversion step in any coal utilization process, has a significant impact on the overall reactor performance. Therefore, special attention should be paid to describe the detailed devolatilization behavior under such extreme operating conditions. Higuera[15] proposed a mathematical model using a competing reaction pyrolysis model, whereas Tian et al.[16] adopted chemical percolation devolatilization (CPD) model to simulate coal devolatilization. Both results showed sound agreement with the experimental data. Chen and Cheng[17] established a comprehensive model incorporating CPD model to describe the complex gas-particle reaction behavior of coal pyrolysis, and the results qualitatively agreed with the major operational experience on the 2-MW pilot-plant reactor.

As is well-known, the inward flow of thermal energy to coal is the key issue for coal devolatilization. However, the heat-transfer resistance inside particles was neglected, and the temperature distribution inside the particle was assumed to be uniform in the above models. To deeply understand the heat transport inside a single coal particle under the extreme environmental conditions, Shuang et al.[18] successfully proposed a mechanism model incorporating the heat conduction in solid materials, diffusion of released volatile gases and reactions. The results demonstrated that both the resistances would impede thermal energy from transporting into the particle and should be considered seriously for such an ultrahigh temperature and ultrafast pyrolysis process.

To further investigate the detailed particle devolatilization behavior and predict the scale-up performance to a 5-MW reactor, the above particle heat-transfer mechanisms (Shuang et al.[18]) has been taken into account in the CFD approach[17] together with the physical models of coal devolatilization, and the tar cracking reactions,[19,20] forming a comprehensive modeling scheme [i.e., CFD with discrete phase model (DPM)]. Here, the improved CPD model[21–23] is applied to describe the devolatilization behavior of rapidly heated coal based on the physical and chemical transformations of the coal structure. The model predictions will be validated with the experimental data under the typical operating conditions from the 2- and 5-MW pilot-plant plasma reactors. Because the practical measurements in a thermal plasma reactor are not realistic, the reactor performance can be alternatively disclosed using the updated CFD-DPM with particle-scale physics. The three-dimensional (3-D) simulation can reveal the detailed flow field, gaseous temperature, distribution of main species, heating-up, and devolatilization process of a single particle, temperature distribution inside coal particles, and so on. Accordingly, fresh understanding on the relationship between the particle trajectory in a 3-D real reactor and corresponding coal devolatilization performance can be achieved. Furthermore, we are aiming to obtain the optimal operating conditions to improve the 5-MW reactor performance and point out the key issues to guide the reactor scale-up.

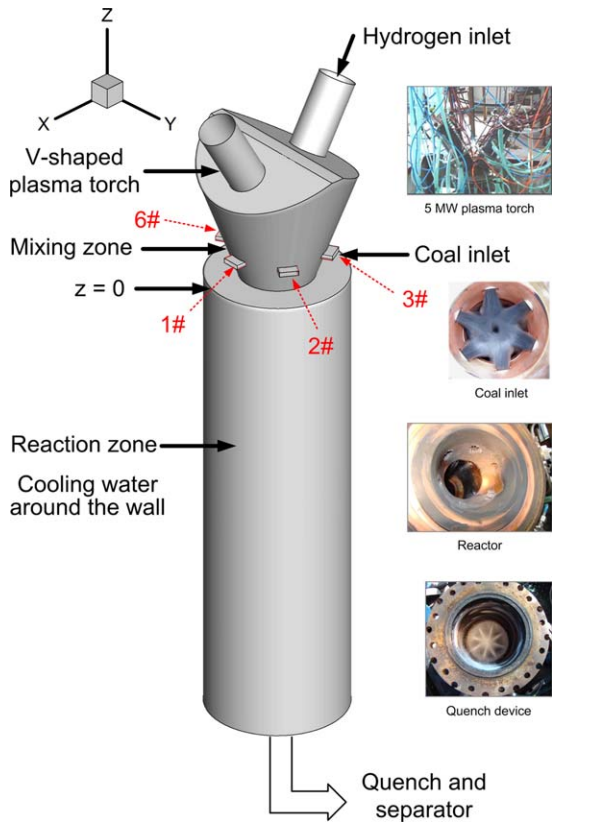

Figure 1. Schematic of the 5-MW/2-MW plasma downer reactor.

[Color figure can be viewed in the online issue, which is available at wileyonlinelibrary.com.]

Pilot-Plant Thermal Plasma Reactor: Design and Practice

Figure 1 shows the schematic drawing of the 5-/2-MW plasma downer reactor for coal pyrolysis, which is composed of the V-shaped plasma torch, mixing section, reaction chamber, quench device, and separator. The V-shaped hydrogen plasma torch was installed at the top of the downer reactor to provide the ultrahigh temperature fluid. The inside diameter of the 5- and 2-MW reaction chamber is 150 and 80 mm, respectively. Because the reaction time is in milliseconds, the length of both downers is very short, that is, only about 500 mm. The mixing zone with six coal injection nozzles and the reaction zone are to guarantee the rapid heating of the coal particles to release the volatiles in milliseconds. The mixing zone is made of copper with water cooling, whereas the reaction chamber is made of porous stainless steel protected by water steam. Coal injections are located at the side wall well below the plasma torch so as not to influence the stability of the DC arc. At the downstream of the reaction zone, there is a quench operation, using water as the quench material, to efficiently prevent the decomposition of acetylene to hydrogen and soot. After that the gas-solid mixture is separated in the separator. Hydrogen jets into the downer reactor from either end of the V-shaped torch. An extra H_2 introduced into the reactor from the coal injections is used to accelerate coal particles. To ensure the

Table 1. Performance of Tianye Pilot-Plant Reactors under Typical Operating Conditions

Input	2-MW	5-MW	Output	2-MW	5-MW
Power (MW)	1.8	4.0	C_2H_2 (v/v %)	8	6.2
System pressure (atm)	1	1	CO (v/v %)	7	10.5
H_2 feed to plasma torch (kg/h)	35	105	CH_4 (v/v %)	4	3.6
H_2 feed to coal inlets (kg/h)	10	23	C_2H_4 (v/v %)	2.5	1.1
Coal feed (kg/h)	700	1700	H_2 (v/v %)	78	77.4

milliseconds mixing between the ultrahigh temperature hydrogen stream and the solids, that is, the rapidly heating of the coal particles, an improved design of coal injection is implemented according to the study by Cheng et al.[24] Represented experimental data obtained from the 2- and 5-MW pilot plant reactors are shown in Table 1.

Mathematical Model

Because the temperature in the computation domain of the downer reactor is far below the point at which the gas starts to ionize, there is actually no electromagnetic field. Therefore, the magnetohydrodynamic model is not included in the simulation. The plasma jet flow is assumed to be a thermal stream of hydrogen with the average temperature, velocity, and the equilibrium compositions of H_2 and H atom. The average temperature of the hot hydrogen can be estimated according to the energy balance of the system. The solid volume fraction in the actual pilot reactor is very low, usually less than 1%. Thus, the particle is considered as a dispersed phase by DPM, where the effects of the particle volume fraction on the gas phase and the particle–particle interactions are neglected.

The yield of acetylene is governed by two crucial steps: coal devolatilization and volatile reactions. Due to the milliseconds contact time, thermal energy is the driving force for coal devolatilization. Therefore, the heat transport inside a coal particle must be modeled in details, and the CFD-DPM approach is established based on the following basic simplifications and assumptions:

1. The coal particles are assumed to be dry, porous spheres with constant diameter, uniform boundary conditions (on surface), and centrosymmetrical variations of local temperature and porosity;
2. The internal mass diffusion of the released volatiles in coal particles is ignored, but considered with an effective particle-based correction for the effect of mass transfer on heat transfer;
3. The temperature of the released volatiles inside a coal particle is assumed to be the same as that of the solids at local position due to strong interphase heat transfer;
4. The thermal effect of ash melting on the temperature of a coal particle is neglected.

Overall, the comprehensive CFD-DPM constructed by using the Cartesian coordinates includes three parts: (1) continuous phase: the k-ε turbulence model for gaseous turbulent flow with heat, mass, and momentum transfers (see Appendix A for these governing equations), the mixture fraction approach with the probability density function (PDF) method for modeling the interaction of turbulence and chemistry, the thermodynamic equilibrium model for high-temperature gas-phase chemical reactions, and the discrete ordinates radiation model for calculating the radiative heat transfer in the reactor; (2) discrete phase: DPM for particle-phase momentum transfer, a heat balance model for temperature distribution inside particle, and submodels for coal devolatilization; (3) the interactions between continuous phase and discrete phase.

Governing equations for continuous phase

Conservation Equations for the Mixture Fraction Approach. The species transport and gaseous chemical reactions are extremely complex in coal pyrolysis process. However, since the gaseous reactions time is about 0.4 ms,[25–27] whereas devolatilization time is 2–10 ms,[28] the mass and heat transfer between the coal particle and heating gas is the rate determining step. Therefore, it is reasonable to assume that once the volatiles are released the gaseous reaction rate is determined by the mixing process of the volatiles with the hot hydrogen. In other words, the mixing time scale is much greater than the reaction time scale in this process. Therefore, the turbulent mixing should be treated in detail while the reaction chemistry is computed using an equilibrium algorithm because of the ultrahigh temperature. Under the assumption of equal diffusivities, the thermochemistry can be reduced to a single parameter, that is, the mixture fraction (denoted by f), which is the mass fraction originated from the primary stream, can be written in terms of the atomic mass fraction as[29]

$$f=\frac{Z_i-Z_{i,\text{second}}}{Z_{i,\text{first}}-Z_{i,\text{second}}} \tag{1}$$

where Z_i is the elemental mass fraction for element, i. The subscript first denotes the value at the primary stream inlet and the subscript second denotes the value at the second stream. If the diffusion coefficients for all species are equal, then Eq. 1 is identical for all elements, and the mixture fraction definition is unique. The assumption is reasonable for turbulent flows where turbulent convection overwhelms molecular diffusion.

This method is computationally efficient in that it does not require the solution of a large number of species transport equations. Instead, species concentrations are derived from the predicted mixture fraction fields. According to the mixture fraction approach, volatiles released from coal and the hot hydrogen are identified as the primary and secondary streams, respectively. Transport equations for the mean (density-averaged) mixture fraction is

$$\frac{\partial}{\partial t}(\rho\bar{f})+\nabla\cdot(\rho\bar{f}\vec{u})=\nabla\cdot\left(\frac{\mu_t}{\sigma_f}\nabla\bar{f}\right)+M \tag{2}$$

The source M is due solely to transfer of mass into the gas phase from the particle phase.

In addition to solving for the mean mixture fraction, the conservation equation for the mixture fraction variance $\overline{f'^2}$, is described as following[30]

$$\frac{\partial}{\partial t}(\rho \bar{f'^2}) + \nabla \cdot (\rho \bar{f'^2} \vec{u}) = \nabla \cdot \left(\frac{\mu_t}{\sigma_g} \nabla \bar{f'^2}\right) + C_g \mu_t (\nabla \bar{f})^2 - C_d \rho \frac{\varepsilon}{k} \bar{f'^2} \quad (3)$$

where

$$f' = f - \bar{f}$$

The default values for the constants C_g and C_d are 2.86 and 2.0, respectively. The mixture fraction variance is used in the closure model describing turbulence–chemistry interactions.

For nonadiabatic systems, under the assumption of chemical equilibrium with the mixture fraction below 0.94 (when the mixture fraction is more than 0.94, the local temperature of gas mixture is probably lower than 1500 K, where the equilibrium chemistry calculation might be no longer applicable. That is to say, the composition is computed using equilibrium for the mixture fraction below this value but based on mixing when it is above this value), all thermochemical scalars (species fractions, density, and temperature) are uniquely related to the instantaneous mixture fraction and enthalpy

$$\phi_n = \phi_n(f, H) \quad (4)$$

Interaction of turbulence and chemistry is accounted for using an assumed-shape PDF (β-PDF), $p(f)$, so the mean scalars are calculated as

$$\bar{\phi}_n = \int_0^1 \phi_n(f, H) p(f) df \quad (5)$$

Governing equations for discrete phase

Equations of Motion for Particles. The trajectory of a discrete phase particle is predicted by integrating the force balance acting on the particle. The force balance is shown as

$$\frac{d\vec{u}_p}{dt} = F_D(\vec{u} - \vec{u}_p) + \frac{\vec{g}(\rho_p - \rho)}{\rho_p} + \vec{F} \quad (6)$$

where $\vec{u}$ is the velocity of continuous phase, $\vec{u}_p$ is the particle velocity, ρ is the fluid density, ρ_p is the density of the particle, $\vec{g}$ is the gravity acceleration, $\vec{F}$ is an additional acceleration (force/unit particle mass) term, $F_D(\vec{u} - \vec{u}_p)$ is the drag force per unit particle mass and

$$F_D = \frac{18\mu}{\rho_p d_p^2} \frac{C_D \mathrm{Re}}{24} \quad (7)$$

Here, μ is the molecular viscosity of the fluid, d_p is the particle diameter, and Re is the relative Reynolds number, which is defined as

$$\mathrm{Re} = \frac{\rho_p d_p |\vec{u}_p - \vec{u}|}{\mu} \quad (8)$$

The drag coefficient, C_D, for the smooth spherical particles can be taken from

$$C_D = a_1 + \frac{a_2}{\mathrm{Re}} + \frac{a_3}{\mathrm{Re}^2} \quad (9)$$

where a_1, a_2, and a_3 are constants that apply over several ranges of Re given by Morsi and Alexander.[31]

Owing to the large temperature gradient in ultrahigh temperature hydrogen plasma jet, the particles injected into the hot gas experience a force in the direction opposite to that of the gradient. This phenomenon is known as thermophoresis. The thermophoretic effect on particles is considered in the additional acceleration term $\vec{F}$, in Eq. 6

$$\vec{F} = -D_{T,p} \frac{1}{m_p T} \nabla T \quad (10)$$

where m_p is the mass of the coal particle and $D_{T,p}$ is the thermophoretic coefficient.

Heat-Transfer Submodel Inside a Coal Particle. As the average gas temperature can reach 3000 K in thermal plasma and the heating rate of particles can reach 10^6 K/s, the whole pyrolysis process finishes in a few milliseconds so that the heat transfer inside a single pulverized coal particle becomes significant. Based on our earlier work,[18] a simplified heat-transfer model within a coal particle is established based on the conduction equation with consideration of the solid material and the volatile gases. Heat transfer to the particle includes contributions from convection, radiation, and the heat consumed during devolatilization

$$(\rho_p c_p)_{\mathrm{eff}} \frac{\partial T_p(r,t)}{\partial t} = \frac{1}{r^2} \frac{\partial}{\partial r} \left(\lambda_{\mathrm{eff}} r^2 \frac{\partial T_p(r,t)}{\partial r}\right) - \Delta_r H \cdot \gamma_{\mathrm{vol}}(r,t) \quad (11)$$

where

$$(\rho_p c_p)_{\mathrm{eff}} = \varphi \rho_{\mathrm{vol}} c_{p,\mathrm{vol}} + (1-\varphi) \rho_s c_{p,s} \quad (12)$$

$$\lambda_{\mathrm{eff}} = \varphi \lambda_{\mathrm{vol}} + (1-\varphi) \lambda_s \quad (13)$$

In these equations, $T_p(r,t)$ represents the local temperature at any radial position r inside a particle and time t, φ is the porosity of particle, ρ_s and ρ_{vol} are the densities of the solid material and the volatile phases, respectively; $c_{p,s}$ and $c_{p,\mathrm{vol}}$ are the specific heat capacities of the solid material and volatile phases, respectively; λ_{eff} is the effective local thermal conductivity; λ_s and λ_{vol} represent the thermal conductivities of the solid material and volatile, respectively. $\Delta_r H$ is the heat of pyrolysis as volatiles are evolved (1.146×10^6 J/kg), $\gamma_{\mathrm{vol}}(r,t)$ denotes to the rate of devolatilization (kg/m^3·s).

The initial conditions are given as

$$T_p(r,0) = T_{p,\mathrm{init}}, \quad \varphi = \varphi_0 (0 \le r \le R) \quad (14)$$

where $T_{\mathrm{p,init}}$ is the initial temperature of the coal particle, φ_0 is the initial porosity of particle, which is estimated 0.284 in this work. During the simulation, the material properties, λ_s and $c_{p,s}$, are estimated with the varying temperature at each local position and each time step. λ_s is treated as a linear fitted function based on the experimental data,[32] as $\lambda_s = 0.23(1 + 0.0033 T_s)$; $c_{p,s}$ is calculated by a method developed by Merrick[33] as a function of T_s.

The boundary conditions are

$$\begin{cases} 4\pi R^2 \lambda_{\mathrm{eff}} \left.\dfrac{\partial T_p}{\partial r}\right|_{r=R} = 4\pi \left(R + \dfrac{\delta_m}{2}\right)^2 h(T - T_w)\theta + \sigma \varepsilon_p (4\pi R^2)(T^4 - T_w^4) \\ \left.\dfrac{\partial T_p}{\partial r}\right|_{r=0} = 0 \end{cases} \quad (15)$$

where R is the radius of the coal particle, T_{w} is the temperature at the surface of the coal particle, T is local temperature of the continuous phase, σ is the Stefan–Boltzmann constant, ε_{p} is the black-body radiation coefficient for the pulverized coal, δ_m is the thickness of the gas film around the coal

Table 2. Chemical Analysis of Long-Flame Coal

Proximate analysis (%)			Ultimate analysis (%)				
Moisture (ad)	Ash (ad)	VM (daf)	C (daf)	H (daf)	N (daf)	S (daf)	O (daf)
2.85	12.34	41.62	78.13	5.00	1.38	0.79	14.70

ad: air dry basis; daf: dry ash free basis.

particle (estimated to be 2R at a relative small Reynolds number in this study), h is the gas-particle heat-transfer coefficient, and θ is a factor related to the effect of volatiles' release on heat conduction.

The gas-particle heat-transfer coefficient could be calculated from the Nusselt number, which is estimated as a function of the operating conditions and material properties,[34]

$$h=\frac{Nu\lambda_m}{d_p} \tag{16}$$

$$Nu=(2.0+0.6\mathrm{Re}_m^{1/2}\mathrm{Pr}_m^{1/3})\left(\frac{\rho\mu_m}{\rho_m\mu}\right)^{0.15} \tag{17}$$

$$\mathrm{Re}_m=\frac{\rho_m d_p|\vec{u}_p-\vec{u}|}{\mu_m} \tag{18}$$

$$\mathrm{Pr}_m=\frac{\mu_m c_{p,m}}{\lambda_m} \tag{19}$$

where d_p represents the diameter of the coal particle and the subscript m denote that the parameters should be calculated with respect to the temperatures of film ($T_m = (T + T_w)/2$).

The factor θ reported by Spalding[35] is adopted in this study

$$\theta=\frac{B}{e^B-1} \tag{20}$$

$$B=\frac{c_{p,m}}{2\pi d_p\lambda_m}\left(\frac{dm_\mathrm{vol}}{dt}\right) \tag{21}$$

where dm_vol/dt denotes the formation rate of volatiles from coal (kg/s).

Coal Devolatilization Model. According to the reaction scheme of coal pyrolysis in hydrogen plasma proposed by Baumann et al.[28] and the analysis of coal particles in the 2-MW/5-MW reactors, devolatilization is believed to be the first essential step of this coal pyrolysis process.

During coal pyrolysis, the labile bonds between the aromatic clusters in the coal structure lattice are cleaved and then result in two general classes of fragments. One set of fragments has a low molecular weight and escapes from coal particle as a light gas. The other set of fragments consists of tar gas precursors that have a relatively high molecular weight and tends to remain in coal particles for a long period of time during typical devolatilization conditions. The portion of the lattice structure that remains after devolatilization is comprised of char and mineral-compound-based ash. The CPD[21–23] model is used to describe the devolatilization of coal particles in this simulation, in which the coal structure is treated as a simplified lattice of aromatic clusters, whereas the light gases, char, and tar precursors are formed from the breakdown of the macromolecular network.

The kinetic parameters and corresponding rate constants for the CPD model are coal independent, which are included in the submodel formulation and are not input or modified during problem setup. While the chemical structure parameters are coal-specific and must be specified during the problem setup. The five parameters are:

initial fraction of bridges in the coal lattice, p_0;
initial fraction of char bridges, c_0;
lattice coordination number, $\sigma + 1$;
cluster molecular weight, $M_{\mathrm{w},1}$;
side chain molecular weight, $M_{\mathrm{w},\delta}$.

The first four of these parameters are coal structure quantities that are obtained from NMR experimental data. The last quantity, representing the char bridges that either exist in the parent coal or are formed very early in the devolatilization process, is estimated based on the coal rank. In this work, the chemical structure parameters are obtained by nonlinear correlations[36] between data from ^{13}C NMR analysis and those from chemical analysis of the long-flame coal from Miquan City, Xinjiang Province of China in this article.

The proximate and ultimate analysis data and the values for the coal-dependent parameters of the coal used in the 2-MW/5-MW pilot plants are shown in Tables 2 and 3, respectively.

At extremely high temperature, the tar precursors escape from the coal particle as tar gases, and then crack into soot and light gases again. However, these reactions are not included in the available CPD model. In our simulations, we make an improvement on the coal devolatilization model by considering the tar cracking reactions through the following assumed paths

$$\mathrm{Lightgases} \xleftarrow{k_1} \mathrm{Tar} \xrightarrow{k_2} \mathrm{Soot}$$

Actually, tar pyrolysis in plasma is not simply divided into such two successive phases, but this acts as a compromise in the modeling scheme. The mechanism uses the Arrhenius equation which is defined as

$$k_i=A_i\exp\left(-\frac{E_i}{RT}\right) \qquad i=1,2 \tag{22}$$

The values of the kinetic parameters are obtained from the work of Ma[19] and Brown.[20] The values used for the preexponential constant A and the activation energy E are listed in Table 4.

The temperature of tar is assumed to be the same as that of the film due to the rapid heat transfer in the gaseous phase. In this simulation, we assume that the remaining tar and soot still remain in the coal particle, the physical properties of which are similar to those of char. Therefore, the mass of coal particle consists of char, tar, and soot. Due to the ultrahigh temperature, the gaseous reaction is computed using an equilibrium algorithm based on the components of volatiles. However, CPD model cannot predict the formation profiles of individual components included in volatiles in coal pyrolysis. The element fractions of volatiles can be specified according to the proximate and ultimate analyses of the coals before and after pyrolysis, as well as the mass

Table 3. Chemical Structure Parameters of Long-Flame Coal for CPD Model

Coal type	$\sigma + 1$	p_0	$M_{w,1}$	$M_{w,\delta}$	c_0
Long-flame coal	5.11	0.57	326.17	36.18	0.031

Table 4. Rate Constants for Tar Cracking Model

Rate constants	A (1/s)	E (kJ/kgmol)
k_1	9.77×10^{10}	2.86×10^5
k_2	5.02×10^8	1.98×10^5

conservation of elements. Similarly, the standard-state enthalpies of pseudospecies volatile can be computed based on energy conservation and the higher/lower heating value of the coal. The evaluation of the devolatilization species released to the continuous phase and the heat of pyrolysis is found reasonable by the method mentioned above.

Interphase exchanges between continuous phase and discrete phase

In the coupled CFD-DPM approach, the discrete phase behaviors are predicted based on the continuous phase flow field, whereas the continuous phase behavior is impacted by the discrete phase. This interphase exchange of momentum, heat, and mass between the particle and the continuous phases is depicted qualitatively in Figure 2.

Momentum Exchange. The momentum transfer from the continuous phase to the discrete phase is computed by examining the change in momentum of a particle as it passes through each control volume. This momentum exchange is computed as

$$\vec{F}=\sum\left(F_D(\vec{u}_p-\vec{u})+\vec{F}_{\text{thermo}}\right)\dot{m}_p\Delta t \tag{23}$$

where $\vec{F}_{\text{thermo}}$ is the thermophoretic force, $\dot{m}_p$ is the mass flow rate of the particles, and Δt is the time step. This momentum exchange appears as a momentum source in the continuous phase momentum balance in any subsequent calculations of the continuous phase flow field.

Heat Exchange. Similarly, the heat exchange is computed as

$$Q=\frac{\dot{m}_{p,0}}{m_{p,0}}\left[\left(m_{p,in}-m_{p,\text{out}}\right)h_{\text{pyrol}}+m_{p,in}\int_{T_{\text{ref}}}^{T_{p,\text{in}}}c_{p,p}dT-m_{p,\text{out}}\int_{T_{\text{ref}}}^{T_{p,\text{out}}}c_{p,p}dT\right] \tag{24}$$

where $\dot{m}_{p,0}$ is the initial mass flow rate of the particle injection (kg/s), the parameters on the cell entry and exit are indicated by the subscripts in and out, respectively. This heat exchange appears as a heat source in the transport equation for mean enthalpy of the continuous phase.

Mass Exchange. The mass exchange is computed simply as

$$M=\frac{\dot{m}_{p,0}}{m_{p,0}}\left(m_{p,\text{in}}-m_{p,\text{out}}\right) \tag{25}$$

This mass exchange appears as a source of mass in the continuity equation of continuous phase and as a source of mass in the transport equation for the mean mixture fraction and the continuity equation.

The strategy of numerical simulation

The numerical simulations of gas-particle flows follow the Eulerian–Lagrangian scheme, as shown in Figure 2. The gas phase is treated as a continuum by solving the Navier–Stokes equations, whereas the particle is considered as the dispersed phase, solved by tracking a large number of particles through the calculated flow field. As the trajectory of each particle is computed, the momentum, mass, and energy exchange between the particles and the gas phase is added to the source term of the gas phase governing equations (see Appendix B for computational details).

The solution of the complex model described above is implemented using the commercial software FLUENT with many self-developed user-defined functions.

The material properties of hydrogen plasma come from Boulos et al.[34] as a function of the temperature, whereas the ones of volatiles are calculated by kinetic theory.[37] The material properties of the mixture in the gas phase are calculated by user-defined mixing law. That is to say, the thermal conductivity and viscosity of the mixture are calculated by $\lambda_{\text{mix}}=\sum\lambda_j x_j M_j^{1/3}/\sum x_j M_j^{1/3}$ and $\mu_{\text{mix}}=\sum\mu_j x_j M_j^{1/2}/\sum x_j M_j^{1/2}$, respectively, where x_j is the molar fraction and M_j is the molar mass of species j. Other properties are calculated by mass-weighted mixing law embedded in FLUENT.

The initial temperature and velocity of coal particles injected transversely from the uniformly distributed nozzles are 300 K and 5 m/s, respectively. The particle-size distribution measured from the industrial coal is fitted into the Rosin–Rammler function

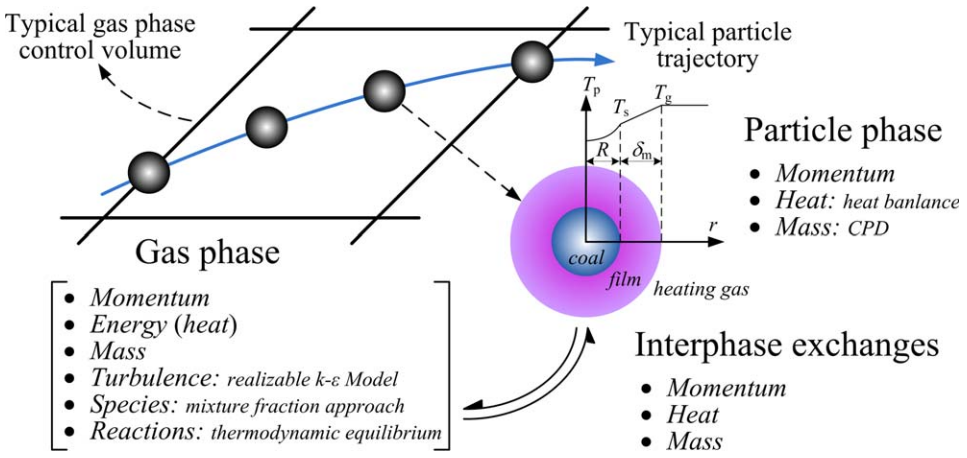

Figure 2. Illustration of the modeling scheme of CFD-DPM approach considering heat, mass, and momentum transfer between the particle and gas phases.

[Color figure can be viewed in the online issue, which is available at wileyonlinelibrary.com.]

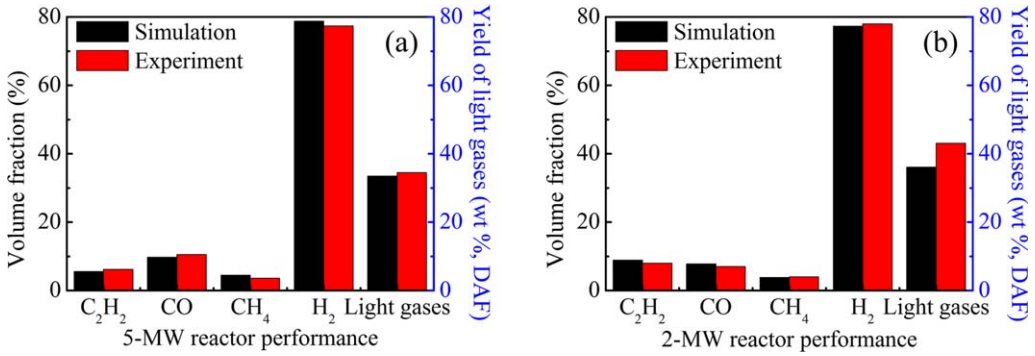

Figure 3. Comparisons of model predictions with experimental data under typical operating conditions shown in Table 11: (a) 5-MW reactor; (b) 2-MW reactor.

[Color figure can be viewed in the online issue, which is available at wileyonlinelibrary.com.]

$$Y_d = e^{-(d/\bar{d})^n} \tag{26}$$

where Y_d is the mass fraction of particles with diameter greater than d; the minimum, maximum, and mean diameters are 6.22, 137.2, and 45.78 μm, respectively; and the spread parameter, n, is 1.0578. The commonly used structured hexahedron mesh generation is adopted for both the 2- and 5-MW reactors. To give acceptable solution accuracy, the grid was refined at the sharp solution features (e.g., around the coal nozzles in the mixing zone, the minimum grid volumes are 1.40×10^{-9} m^3 for the 2-MW reactor, whereas 2.60×10^{-9} m^3 for the 5-MW reactor). In contrast, the last 200–300 mm of the reactor chamber (near the outlet) in which the solution was very smooth, where the grid was coarsened (e.g., the maximum grid volumes are 1.30×10^{-7} m^3 for the 2-MW reactor, whereas 3.86×10^{-7} m^3 for the 5-MW reactor), leading to acceptable accuracy with a decrease in solution time. The total grid numbers in the computational domain of the 2- and 5-MW reactors are 232,541 and 218,456, respectively. The equiangle skew of 93% grids in both computational domains is no more than 0.3 and the maximum value is below 0.5. According to the heat-transfer conditions of industrial reactors, the convective heat-transfer boundary condition is applied at the wall of mixing zone, the external heat-transfer coefficient, and external heat sink temperature are given as 3000 W/m^2·K and 300 K, respectively, although a fixed temperature of 1500 K is specified at the wall of the reaction chamber.

Results and Discussion

Model validation

The predicted volume fractions of main species and total yield of light gases at the outlet (we defined the plane z = −0.5 m as the "outlet," not the actual outlet of the reactor) of the reactors using these two practical geometries are plotted in Figure 3, together with the corresponding experimental data. The light gases refer to the products in the gaseous state under normal temperature and pressure, and yield of light gases is defined as the ratio of the mass flow rate of the light gases to the feed rate of coal particles (dry ash free basis) in this article. The predictions and the actual performance of the 2- and 5-MW pilot reactors are based on the typical operating conditions shown in Table 1. For the inherent difficulty in practical measurement, more detailed experimental data in the reactor cannot be obtained. It can be seen from Figures 3a, b that the model predictions agree well with the experimental data in both reactors in spite of the quench process was not considered in this model. This might also shows that the quenching effect is excellent in the practical pilot reactors. On the other hand, the predicted volume fraction of C_2H_2, which represents the reactor performance, is much lower at the outlet of the 5-MW reactor compared to the 2-MW reactor. The similar trend is also found in the actual situation during the scale-up process. Therefore, this comprehensive CFD-DPM is capable of describing the complex gas-particle reaction behavior in the pilot-plant reactors under a wide range of operating conditions. The simulations can help to understand the reason which results in the different performances of the two sets of pilot-plant facilities. Accordingly, we try to illustrate the interested particle-scale behaviors in the practical reactor. Then, the improved understanding is expected to help optimize the operating conditions and reactor design to improve the 5-MW reactor performance.

The necessity of tar cracking model

In a real process of coal devolatilization at extremely high temperature (e.g., greater than 1600 K), the tar precursors, once formed, may crack into other chemicals whether they

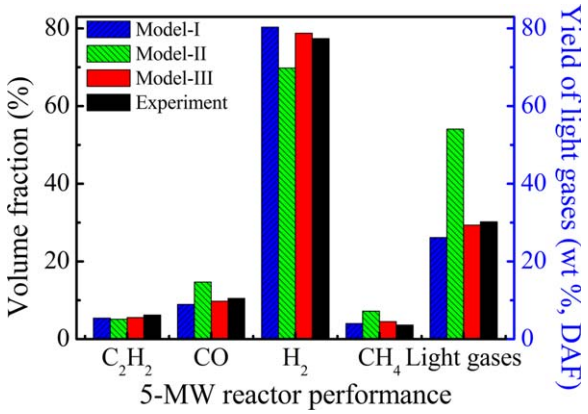

Figure 4. Comparisons of the predicted performance using different tar cracking models with experimental data of the 5-MW reactor.

[Color figure can be viewed in the online issue, which is available at wileyonlinelibrary.com.]

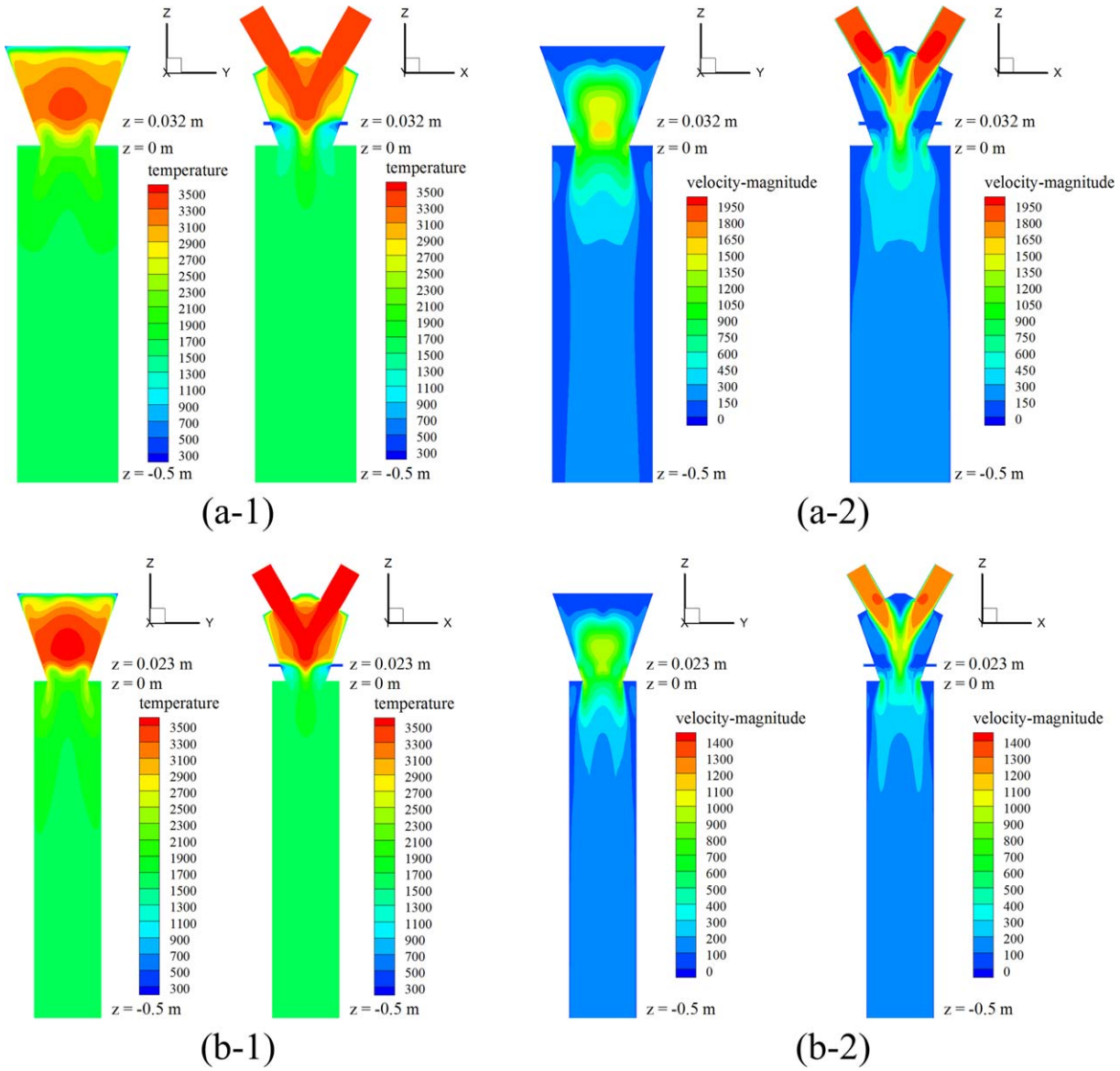

Figure 5. Distribution of (1) gas temperature and (2) velocity magnitude in $x = 0$, $y = 0$ planes: (a) 5-MW reactor; (b) 2-MW reactor.

[Color figure can be viewed in the online issue, which is available at wileyonlinelibrary.com.]

escape from the coal particle as tar gases or tend to remain in the coal. The tar cracking reactions will affect both the yield of volatiles and reactor performance. As described in the section of "Coal devolatilization model," coal pyrolysis in plasma is simply divided into such two successive phases as a compromise in the modeling scheme. Three tar cracking models are carried out to investigate the influences of tar cracking reactions on the performance of the 5-MW reactor:

1. Model-I: the tar cracking reactions is not considered;
2. Model-II: all of the tar converts to light gas, in other words, tar is treated as light gases;
3. Model-III: the tar cracking reaction described in Eq. (22) is considered.

Figure 4 plots the predicted volume fractions of main species and yield of light gases as well as the experimental data at the outlet of the reactor under the operating conditions (see Table 1) from the 5-MW plasma reactor. It can be found that different tar cracking models lead to different devolatilization performances. Compared to Model-I and Model-II, the predictions by Model-III are much closer to the experimental results. This indicates that the effect of tar cracking reactions on the yield of light gases and reactor performance during the devolatilization process should be paid enough attention to. In addition, the comparison showed in Figure 4 also demonstrates the mechanism of tar cracking adopted in this model is applicable for the coal pyrolysis system.

Detailed unmeasurable information of continuous phase

Gas Temperature and Velocity Fields. Figure 5 illustrates the distributions of gas temperature and velocity magnitude in $x = 0$, $y = 0$ planes of both reactors. The six coal inlets are located at $z = 0.035$ m of the 5-MW reactor,

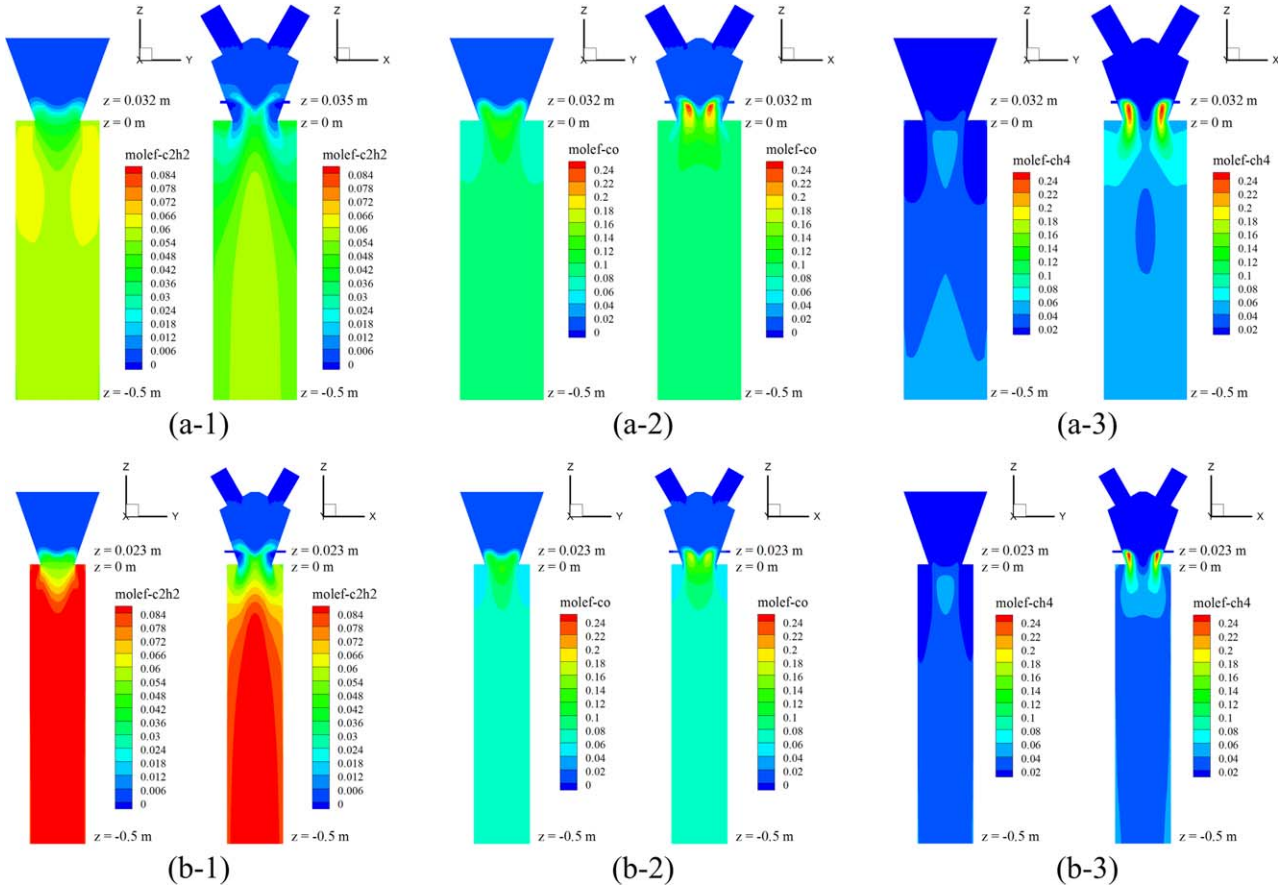

Figure 6. Concentration distribution of (1) C_2H_2, (2) CO, and (3) CH_4 in $x = 0$, $y = 0$ planes: (a) 5-MW reactor; (b) 2-MW reactor.

[Color figure can be viewed in the online issue, which is available at wileyonlinelibrary.com.]

whereas at $z = 0.023$ m of the 2-MW reactor. The temperature distribution in both reactors is similar: the gas temperature changes dramatically after the coal is injected into the reactor and then becomes relative uniform especially after the first 100 mm under the inlet plane. As a consequence of coal injection, there are low-temperature regions adjacent to

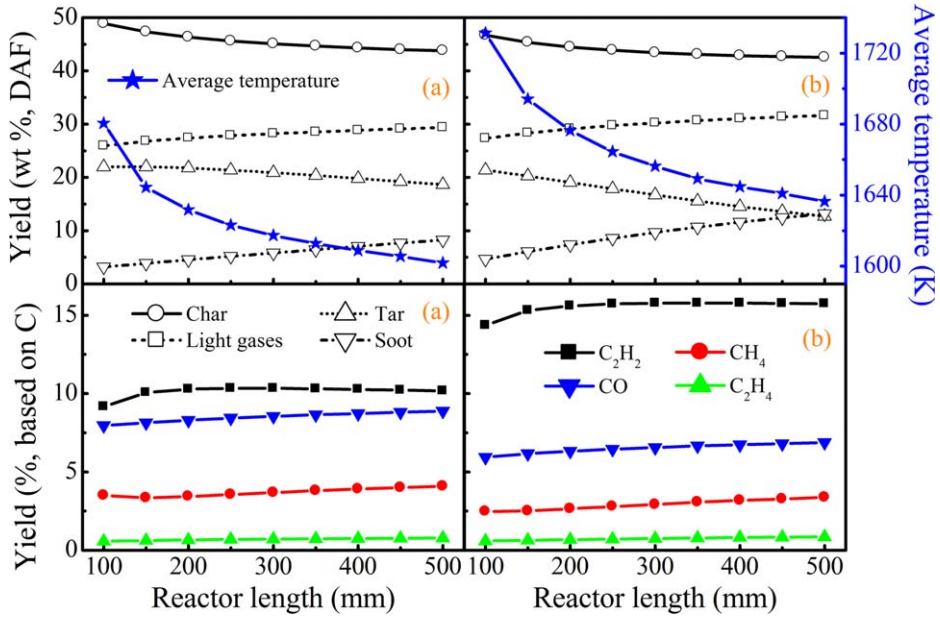

Figure 7. Variation of the yields of products from coal (based on stream mass flow rate), main gaseous species (based on carbon flow rate), and average gas temperature with reactor length: (a) 5-MW; (b) 2-MW.

[Color figure can be viewed in the online issue, which is available at wileyonlinelibrary.com.]

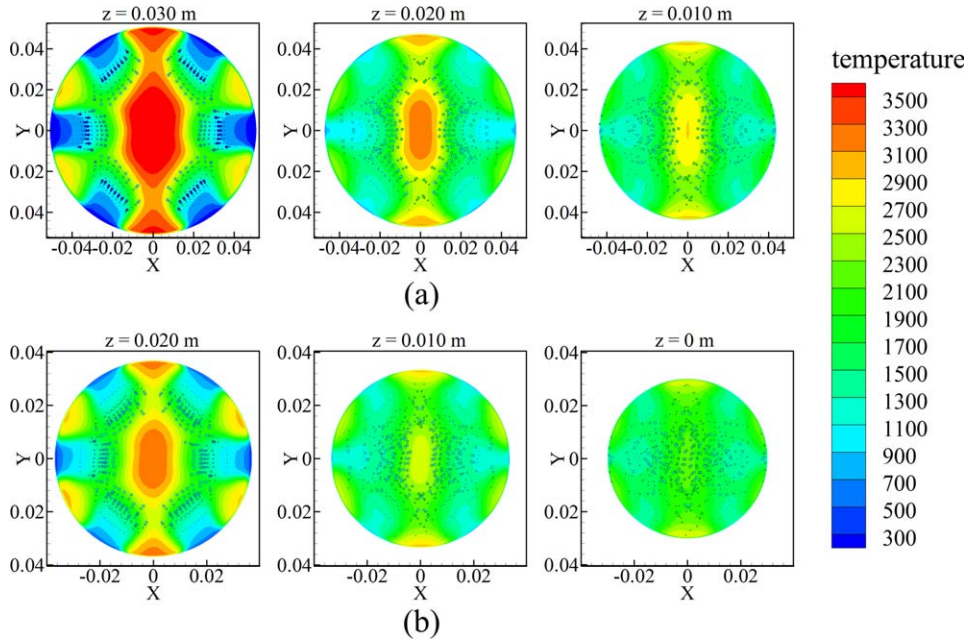

Figure 8. Distribution of coal particles together with the gas temperature field in a series of planes perpendicular to Z axis: (a) 5-MW reactor; (b) 2-MW reactor.

[Color figure can be viewed in the online issue, which is available at wileyonlinelibrary.com.]

the wall below the coal injections, which may be the cause of coking because coal particles become sticky at low temperatures especially when the volatiles are not completely released.

The unique structure of V-shaped torch and the injection of coal particles causes a narrow high-speed area in the center of the mixing zone, where the maximum velocity reaches as high as 1616 m/s (the local temperature is 3050 K and the local Mach number is 0.939 with a speed of sound of 1721 m/s) in the 5-MW reactor and 985 m/s (the local temperature is 3548 K and the local Mach number is 0.517 with a speed of sound of 1908 m/s) in the 2-MW reactor, as shown in Figures 5a2, b2). In the case of the 5-MW reactor, the mean temperature is 1602 K and the average velocity of gas is 189 m/s at the outlet. Although at the outlet of the 2-MW reactor, these two parameters are 1636 K and 165 m/s, respectively. There is not much difference between the two parameters. However, the average velocity at the inlet plane is 419 m/s in the 2-MW reactor, but 609 m/s in the 5-MW reactor. Such a high speed of hydrogen may lead to the result that the coal particle cannot be injected into the high-temperature zone of the plasma jet, and then cause a worse reactor performance of the 5-MW reactor. This suggests that the mixing efficiency should be improved during the reactor scale-up.

Distributions of Main Gaseous Species. Figure 6 shows the concentration distributions of C_2H_2, CO and CH_4 in $x = 0$, $y = 0$ planes of both reactors. The concentration distributions of these three species are similar in the two reactors. The concentration of C_2H_2 grows along the reactor length and reaches its peak in the vicinity of the outlet plane. The concentration of CO is more uniformly distributed throughout the downer, except that there is a high-concentration annular region under the coal inlet plane. Similarly, a high-concentration annular region of CH_4 exists near the expansion part, that is, the high-devolatilization rates zone in the reactor. It can be seen from Figures 6a1, b1 obviously that the concentration of C_2H_2 in the 2-MW reactor is higher than that in the 5-MW reactor at the corresponding zone, whereas the trend of CO is opposite, which is consistent with the actual performance of these two reactors.

The yields of products from coal (i.e., char, light gases, tar, and soot, based on ratio of stream mass flow rate) as a function of the reactor length are shown in Figure 7, together with the variation of the yields of the main gaseous species (i.e., C_2H_2, CO, CH_4 and C_2H_4, based on carbon flow rate). The maximum yield of C_2H_2 in the 2-MW reactor reaches 15.8%, which is much higher than that (10.3%) in the 5-MW reactor. As shown in Figure 7, it is observed in both reactors that a very fast conversion, as well as relative high yields of tar, C_2H_2, CO, CH_4 and other products, is achieved in the first 100 mm of the reaction chamber. After that the yields of main products change slightly: the yields of char and tar decrease whereas those of light gases and soot increase with the increase of the reactor length; the yields of CO and CH_4 keep on a steady value, whereas that of C_2H_2 has a maximum value at the reactor length of 200 mm. The average temperature of gas in both reactors decreases monotonously when the reactor length increases from 100 to 500 mm. It can be seen from Figure 7 that coal devolatilization and gaseous reactions almost finish in the first 200 mm of the reactor, which is in accordance with the industrial experience that the 2-MW experimental results stay almost unchanged in total output and product compositions when the last 300 or 400 mm part of the downer is removed.

Detailed particle-scale behaviors of discrete phase

Distribution of Coal Particles in the Reactor. The distribution of coal particles with the diameter less than 65 μm but the mass fraction more than 82.8% is shown in Figure 8, together with the gas temperature field in a series of planes perpendicular to Z axis. It can be seen that the temperature distribution is not uniform in the vicinity of the inlet plane of both two reactors. The narrow, high-temperature zone in

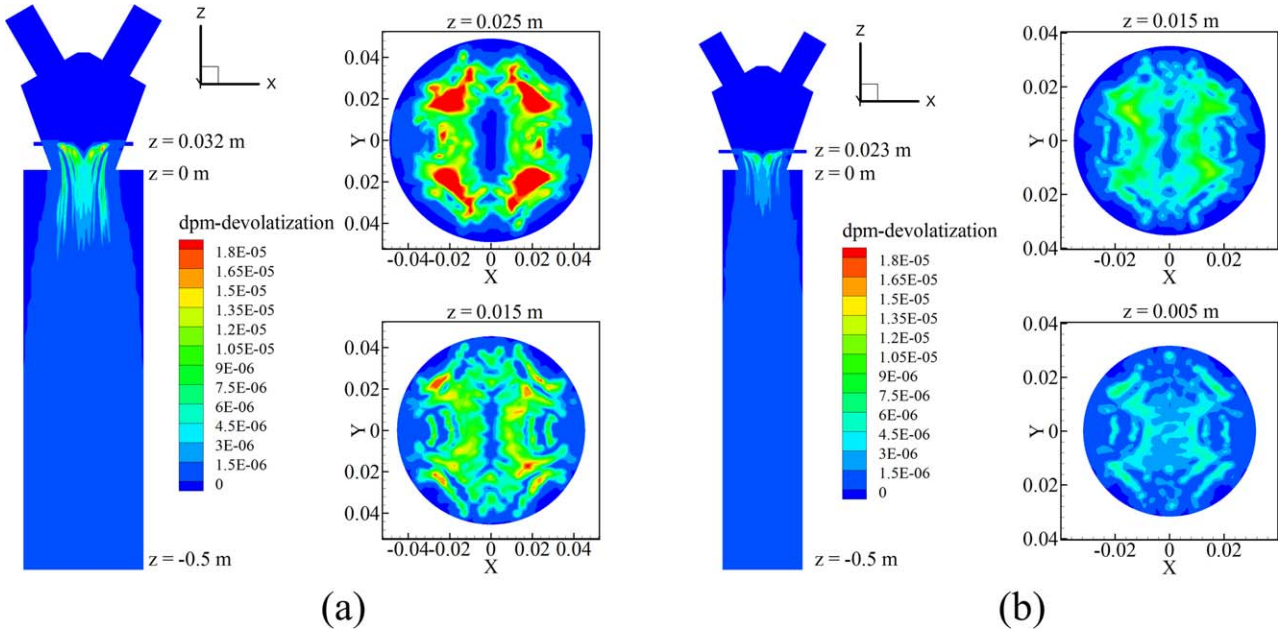

Figure 9. Distribution of particle devolatilization rates in $y = 0$ and a series of planes perpendicular to Z axis: (a) 5-MW reactor; (b) 2-MW reactor.

[Color figure can be viewed in the online issue, which is available at wileyonlinelibrary.com.]

the center is caused by the distribution of coal particles and the unique structure of V-shape torch, whereas the low-temperature regions adjacent to the wall under the inlet plane are the consequence of coal injections. Due to the high-speed heating gas and the reactor geometry, the particles with diameter less than 65 μm can hardly be injected into the center zone within the first 20 mm under the inlet of the 5-MW reactor, whereas the situation in the 2-MW reactor is much better, as shown in Figure 8. The temperature distribution is relatively uniform in the plane of 20 mm below coal injections of the 2-MW reactor, but there is still a larger high-temperature zone in the same place of the 5-MW reactor. The difference means that the gas-particle mixing efficiency gets worse in the 5-MW reactor, then results in a worse reactor performance. It can be found from Figure 8 that to alter the shape of the coal inlet plane or to increase the particle velocity to reduce the injected depth might be an effective way to improve the mixing efficiency.

Distribution of Particle Devolatilization Rates. Figure 9 shows the distribution of particle devolatilization rates in the 5- and 2-MW reactors. The greater rates of both reactors occur in the annular region under the coal inlet plane where the temperature is high and the speed of gas is not very high. The V-shaped geometry also leads to nonuniformity in the distribution of particle reaction rates. Compared to the 5-MW reactor, the devolatilization rates in the planes under the coal inlet plane of the 2-MW reactor are more uniform because of the better distribution of the coal particles. It

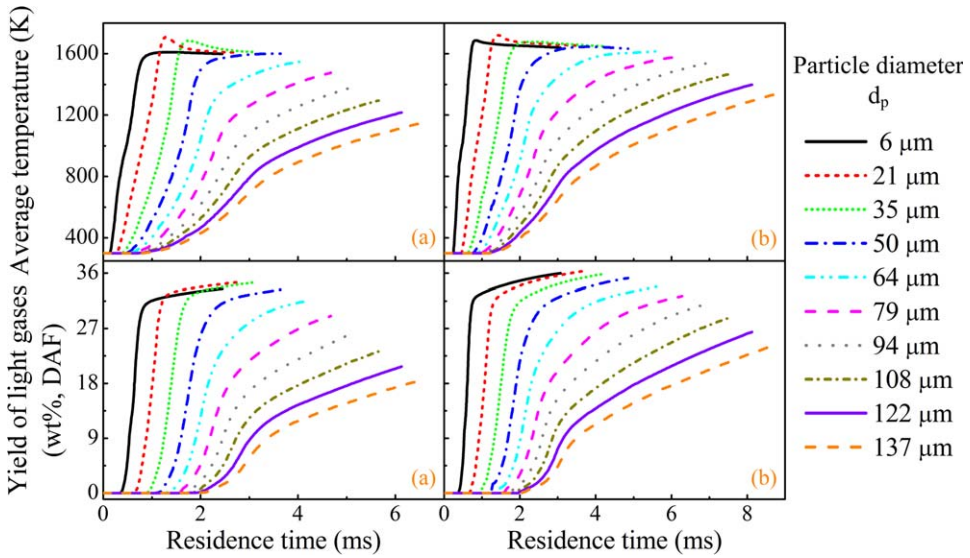

Figure 10. Variations of average particle temperature and yield of light gases with residence time of single representative particle at different particle diameters: (a) 5-MW reactor; (b) 2-MW reactor.

[Color figure can be viewed in the online issue, which is available at wileyonlinelibrary.com.]

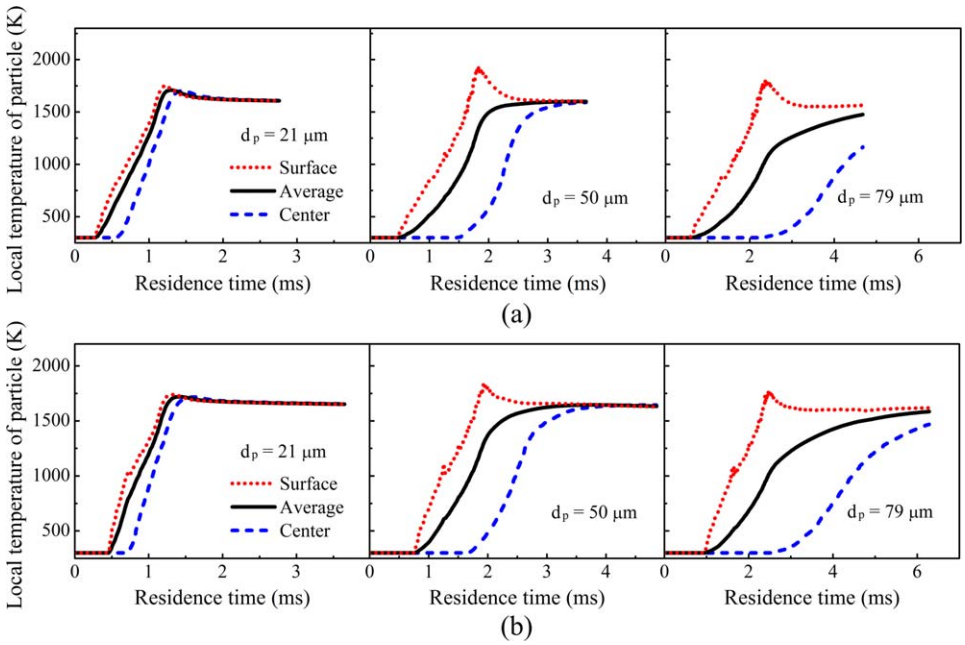

Figure 11. Variations of local particle temperature (surface, center, and average) with residence time at different particle diameters: (a) 5-MW reactor; (b) 2-MW reactor.

[Color figure can be viewed in the online issue, which is available at wileyonlinelibrary.com.]

seems that the particles injected from the inlet 1# and 4# (see in Figure 1, which parallel to the V shape plasma torch) tend to penetrate into the center harder and release the volatiles in the central region at a later time, whereas those injected from the other four inlets release the volatiles more easily and faster. Therefore, the distribution of particle devolatilization rates in the planes parallel to the inlet plane seems to be divided into four symmetric regions, as shown in Figure 9. Figure 9 also illustrates the conclusion that the coal finishes its most reactions in the first 100 mm of the reaction chamber. So the results of the total output and product compositions are improved slightly along the last 400 mm part of the reactor. This is a very important guidance to improve the existing reactor design.

Reaction process of single particles

Different particle sizes directly lead to different particle residence time and heating-up process, resulting in different devolatilization performance, as shown in Figure 10. The particle with smaller diameters is more rapidly heated and has higher particle temperature at the same residence time no matter in the 5-MW reactor or 2-MW reactor. Besides, the residence time of particles grows with the increasing diameter as shown in Figure 10. When the particle diameter is less than 50 μm, the ultimate particle temperature can reach the temperature of the surrounding heating gas; but once larger than 50 μm, larger particle diameter would lead to lower ultimate particle temperature even though the bigger coal particles experience a longer reaction process. For example, in the case of the 2-MW reactor, the temperature of the 50 μm coal particle finally reaches 1633 K with the residence time of 4.9 ms, whereas that of the 137 μm particle just gets to 1333 K within 8.7 ms. The average residence time of particles in the full length of the 5-MW reactor is as short as 4.4 ms, whereas that in the 2-MW reactor reaches 5.7 ms. Correspondingly, the average yield of light gases from coal in the 5- and 2-MW reactors are 29.4 and 31.6%, respectively.

It can be found from Figure 10 that faster heating rate, higher particle temperature, and longer residence time would lead to higher yield of light gases. Therefore, the yield of light gases is relative low for a large-size particle with a relative low-average particle temperature at the same reaction time. The particle temperature and devolatilization rate are mainly determined by the temperature of the surrounding heating gas and the resistant factors of heat conduction and mass diffusion inside the particle.[18] It can be found that integrated effect of the above two resistant factors become more distinct when the particle diameter is larger than 50 μm, which leads to a relative low-devolatilization rate and worse performance. The devolatilization performance of the particles with the same diameter in the 2-MW reactor is better than that in the 5-MW reactor; besides, the larger the particle diameter the bigger the difference.

For further illustration of the effect of the transport resistance on particle heating-up process, the variations of local particle temperature (surface, center, and average) with particle residence time at different particle diameters are plotted in Figure 11. As shown in Figure 11, when the particle diameter is less than 21 μm, it takes about 0.25 ms to transfer heat from the surface into the centre region in the coal particle, which indicates that the resistance of heat conduction and mass diffusion inside the particle is not distinct. That is to say, the temperature distribution inside the particle can be ignored. But when the particle size is large (e.g., >50 μm), though the surface temperature of the particle is very high (because this particle can easily inject into the hot zone), heat could not be transferred efficiently into the center region in the coal particle in the first 1.5 ms or even more time due to the transport resistance that plays a key role to impede the heat transfer inside the particle. This effect would become more obvious when the particle size is larger.

It takes about 3.0 ms to get to a uniform temperature distribution for the 50 μm particles, whereas more than 5.0 ms for the particles with the diameter lager than 79 μm. The maximum temperature difference between the particle center and surface may reach up to 1000 K when the particle diameter is large than 50 μm. Therefore, it can be concluded from Figure 11 that both heat- and mass-transfer resistances should be considered seriously for such an ultrahigh temperature and ultrafast pyrolysis process when the particle size is larger than 50 μm.

Because too large particles are hard to be heated rapidly while those too small can hardly be injected into the high-temperature zone and easily lead to coking on the wall under the injections, the optimal particle diameter for this process is suggested to be 20–50 μm according to above simulation results.

Conclusions

A comprehensive CFD-DPM has been established to describe the complex gas-particle reacting flow of coal pyrolysis, which takes place under ultrahigh temperature with millisecond(s) reaction time in hydrogen plasma reactors. With the significant improvements on the previous work,[17,18] the model predictions are shown to be in good agreement with the performances of both pilot-plant reactors and conclude that an appropriate tar cracking mechanism should be considered for such an ultrahigh temperature and ultrafast pyrolysis process.

The 3-D simulations reveal the detailed unmeasurable distributions of gas temperature, velocity, and main species as well as the detailed particle-scale behaviors, indicating that coal devolatilization and gaseous reactions almost finish in the first 100 mm of the reaction chamber and the difference of average speed at the inlet plane leads to different mixing efficiency. Besides, faster heating rate, higher particle temperature, and longer residence time would lead to higher yield of light gases. The obstacle of internal heat conduction and volatiles diffusion inside the particle can be ignored when the particle diameter is less than 21 μm; but when larger than 50 μm, these two resistances play key roles to impede the heat transfer inside the particle.

The comparison of the two reactors concludes that the cause of unsatisfactory performance in the 5-MW reactor can be attributed to the worse gas-particle mixing efficiency and shorter residence time, which can be improved by adopting a new design of the mixing zone and optimizing the operating conditions. According to the simulation result, the optimal particle diameter for this process is suggested to be 20–50 μm, and the corresponding optimal residence time is about 3 ms to make sure all the particle are completely heated. The future work would provide more scientific guidance on the industrial scaling-up strategy and optimization of process conditions of the coal pyrolysis project at the pilot-plant of 5–10 MW.

Acknowledgments

Financial supports from the National Basic Research Program of China (973 Program no. 2012CB720301), the National Natural Science Foundation of China (NSFC) under grant nos. 20976091 and 20990223, the National Institute of Clean-and-low-carbon Energy (NICE), and Xinjiang Tianye (Group) Co. Ltd. are acknowledged.

Literature Cited

1. Yan BH, Lu W, Cheng Y. China goes green: cleaner production of chemicals. *Green Process Synth.* 2012;1:33–48.
2. Bond RL, Ladner WR, Mcconnell GIT, Galbraith IF. Production of acetylene from coal, using a plasma jet. *Nature.* 1963;200:1313–1314.
3. Bond RL, Ladner WR, Mcconnel. GIT. Reactions of coal in a plasma jet. *Fuel.* 1966;45:381–395.
4. Nicholson R, Littlewood K. Plasma pyrolysis of coal. *Nature.* 1972;236:397–400.
5. Graves RD, Kawa W, Hiteshue RW. Reactions of coal in a plasma jet. *Ind Eng Chem Process Des Dev.* 1966;5:59–62.
6. Gannon RE, Krukonis VJ, Schoenbe. T. Conversion of coal to acetylene in arc-heated hydrogen. *Ind Eng Chem Process Des Dev.* 1970;9:343–347.
7. Chakravartty SC, Dutta D, Lahiri A. Reaction of coals under plasma conditions—direct production of acetylene from coal. *Fuel.* 1976;55:43–46.
8. Bittner D, Baumann H, Klein J. Relation between coal properties and acetylene yield in plasma pyrolysis. *Fuel.* 1985;64:1370–1374.
9. Fauchais P, Bourdin E, Aubreton J, Amouroux J. Plasma chemistry and its applications to the synthesis of acetylene from hydrocarbons and coal. *Int Chem Eng.* 1980;20:289–305.
10. Chakravartty SC, Dixit LP, Srivastava SK. Hydrogen enriched plasma for direct production of acetylene from coal. *Indian J Technol.* 1984;22:146–150.
11. Plotczyk WW, Resztak A, Szymanski A. Plasma processing of brown coal. *Int J Mater Prod Tec.* 1995;10:530–540.
12. Patrick Jr. AJ, Gannon RE. 1 MW prototype arc reactor for processing coal to chemicals. In: Cheremisinoff PN, Farah OG, Ouellette R, editors. Radio Frequency/Radiation and Plasma Processing. Lancaster, PA: Technomic Publishing Inc., 1985:144–154.
13. Kushner LM. Plasma technology in acetylene production in the U. S. In: Cheremisinoff PN, Farah OG, Ouellette R editors. Radio Frequency/Radiation and Plasma Processing. Lancaster, PA: Technomic Publishing Inc., 1985:193–207.
14. Yan BH, Wu CN, Jin Y, Cheng Y. CFD simulation of the reacting flow process of coal pyrolysis to acetylene in hydrogen plasma downer reactors. In: Kim SD, Kang Y, Lee JK, Seo YC editors. New Paradigm in Fluidization Engineering. Korea, 2010:725–732.
15. Higuera FJ. Numerical simulation of the devolatilization of a moving coal particle. *Combust Flame.* 2009;156:1023–1034.
16. Tian YJ, Xie KC, Zhu SY, Fletcher TH. Simulation of coal pyrolysis in plasma jet by CPD model. *Energ Fuel.* 2001;15:1354–1358.
17. Chen J, Cheng Y. Process development and reactor analysis of coal pyrolysis to acetylene in hydrogen plasma reactor. *J Chem Eng Jpn.* 2009;42:103–110.
18. Shuang Y, Wu CN, Yan BH, Cheng Y. Heat transfer inside particles and devolatilization for coal pyrolysis to acetylene at ultrahigh temperatures. *Energy Fuels.* 2010;24:2991–2998.
19. Ma J. Soot formation and soot secondary reactions during coal pyrolysis. Ph.D. Thesis, Utah: Brigham Young University, 1996.
20. Brown AL. Modeling soot in pulverized coal flames. MSc thesis, Utah: Brigham Young University, 1997.
21. Grant DM, Pugmire RJ, Fletcher TH, Kerstein AR. Chemical-model of coal devolatilization using percolation lattice statistics. *Energy Fuels.* 1989;3:175–186.
22. Fletcher TH, Kerstein AR, Pugmire RJ, Grant DM. Chemical percolation model for devolatilization.2. *Temperature and heating rate effects on product yields. Energy Fuels.* 1990;4:54–60.
23. Fletcher TH, Kerstein AR, Pugmire RJ, Solum MS, Grant DM. Chemical percolation model for devolatilization .3. Direct use of c-13 NMR data to predict effects of coal type. *Energy Fuels.* 1992;6:414–431.
24. Cheng Y, Chen JQ, Ding YL, Xiong XY, Jin Y. Inlet effect on the coal pyrolysis to acetylene in a hydrogen plasma downer reactor. *Can J Chem Eng.* 2008;86:413–420.
25. Fincke JR, Anderson RP, Hyde T, Detering BA, Wright R, Bewley RL, Haggard DC, Swank WD. Plasma thermal conversion of methane to acetylene. *Plasma Chem Plasma P.* 2002;22:105–136.
26. Slovetskii DI, Mankelevich YA, Slovetskii SD, Rakhimova TV. Mathematical modeling of the plasma-chemical pyrolysis of methane. *High Energ Chem.* 2002;36:44–52.
27. Beiers HG, Baumann H, Bittner D, Klein J, Juntgen H. Pyrolysis of some gaseous and liquid hydrocarbons in hydrogen plasma. *Fuel.* 1988;67:1012–1016.

28. Baumann H, Bittner D, Beiers HG, Klein J, Juntgen H. Pyrolysis of coal in hydrogen and helium plasmas. *Fuel*. 1988;67:1120–1123.
29. Sivathanu YR, Faeth GM. Generalized state relationships for scalar properties in non-premixed hydrocarbon/air flames. *Combust Flame*. 1990;82:211–230.
30. Jones WP, Whitelaw JH. Calculation methods for reacting turbulent flows: a review. *Combust Flame*. 1982;48:1–26.
31. Morsi SA, Alexander AJ. An investigation of particle trajectories in two phase flow systems. *J Fluid Mech*. 1972;55:193–208.
32. Badzioch S, Field MA, Gregory DR. Investigation of temperature variation of thermal conductivity + thermal diffusivity of coal. *Fuel*. 1964;43:267–280.
33. Merrick D. Mathematical-models of the thermal-decomposition of coal .2. Specific-heats and heats of reaction. *Fuel*. 1983;62:540–546.
34. Boulos MI, Fauchais P, Pfender E. Thermal Plasma. New York: Plenum Press, 1994.
35. Spalding DB. Some Fundamentals of Combustion. London: Butterworths Scientific Publications, 1955.
36. Genetti D, Fletcher TH, Pugmire RJ. Development and application of a correlation of (13)C nmr chemical structural analyses of coal based on elemental composition and volatile matter content. *Energy Fuels*. 1999;13:60–68.
37. Kauzmann W. Kinetic Theory of Gases. New York: W.A. Benjamin, 1966.

Appendix A: Governing Equations

Mass conservation equation (i.e., continuity equation)

The equation for conservation of mass is given as following in Cartesian coordinates

$$\frac{\partial \rho}{\partial t}+\nabla\cdot(\rho\vec{u})=M \tag{A1}$$

where ρ is the density of continue phase, t is time, and $\vec{u}$ is the fluid velocity vector. The source M is the mass added to the continuous phase from the dispersed second phase.

Momentum conservation equation

The Boussinesq's turbulent viscosity hypothesis is used to turbulence modeling; the conservation of momentum in an inertial reference frame is described by

$$\frac{\partial}{\partial t}(\rho\vec{u})+\nabla\cdot(\rho\vec{u}\vec{u})=-\nabla p+\nabla\cdot\left\{(\mu+\mu_t)\left[(\nabla\vec{u}+\nabla\vec{u}^T)-\frac{2}{3}\nabla\cdot\vec{u}I\right]-\frac{2}{3}\rho kI\right\}+\rho\vec{g}+\vec{F} \tag{A2}$$

where p is the static pressure, μ is the molecular viscosity, I is the unit tensor, $\rho\vec{g}$ is the gravitational body force, $\vec{F}$ is the external body force that arise from interaction with the dispersed phase, and μ_t is the turbulent viscosity, which is computed by combining k and ε in the realizable k-ε turbulence model.

Energy conservation equation (i.e., transport equation for the total enthalpy)

When the mixture fraction approach is adopted, determination of $\bar{\phi}_n$ in the nonadiabatic system requires solution of the modeled transport equation for the total enthalpy

$$\frac{\partial}{\partial t}(\rho H)+\nabla\cdot(\rho H\vec{u})=\nabla\cdot\left(\frac{k_t}{c_p}\nabla H\right)+Q \tag{A3}$$

where Q accounts for source terms due to heat exchange with the particle phase and heat transfer by radiation, k_t and c_p are the turbulent thermal conductivity and the specific heat capacity of the continue phase, respectively. The total enthalpy H is defined as

$$H=\sum_j Y_j H_j \tag{A4}$$

where Y_j is the mass fraction of species j and

$$H_j=\int_{T_{\mathrm{ref},j}}^{T} c_{p,j}dT+h_j^0(T_{\mathrm{ref},j}) \tag{A5}$$

where $c_{p,j}$ is the specific heat capacity of species j, and $h_j^0(T_{\mathrm{ref},j})$ is the formation enthalpy of species j at the reference temperature $T_{\mathrm{ref},\,j}$.

Transport equation for the realizable k-ε model

The turbulence kinetic energy k and its rate of dissipation ε in the realizable k-ε model are obtained from the following transport equations

$$\frac{\partial}{\partial t}(\rho k)+\nabla\cdot(\rho k\vec{u})=\nabla\cdot\left[\left(\mu+\frac{\mu_t}{\sigma_k}\right)\nabla k\right]+G_k-\rho\varepsilon \tag{A6}$$

and

$$\frac{\partial}{\partial t}(\rho\varepsilon)+\nabla\cdot(\rho\varepsilon\vec{u})=\nabla\cdot\left[\left(\mu+\frac{\mu_t}{\sigma_\varepsilon}\right)\nabla\varepsilon\right]+\rho C_1 S\varepsilon-\rho C_2\frac{\varepsilon^2}{k+\sqrt{v\varepsilon}} \tag{A7}$$

where

$$C_1=\max\left[0.43,\frac{\eta}{\eta+5}\right],\quad \eta=S\frac{k}{\varepsilon}$$

In these equations, G_k represents the generation of turbulence kinetic energy due to the mean velocity gradients, S is a scalar measure of the deformation tensor, and v is the turbulent kinematic viscosity. C_2 and C_1 are constants; σ_k and σ_ε are the turbulent Prandtl numbers for k and ε, respectively. The model constants C_2, σ_k, and σ_ε have been established to ensure that the model performs well for certain canonical flows, which have the following default values

$$C_2=1.9,\ \sigma_k=\quad 1.0,\ \sigma_e=1.2$$

Appendix B: Computational Details

To fully consider the interaction between phases, the following steps are performed in a coupled two-phase simulation:

1. Solve the gas phase until a partially converged gas-phase flow field is achieved.
2. Introduce the particle phase and calculate the trajectories, temperature, and mass for each particle. The temperature and material properties of gas phase in the boundary condition (Eq. 15) for gas-particle heat-transfer model is obtained from the control volume where the particle stays.
3. Recalculate the gas-phase flow, considering the interphase exchange of momentum, heat, and mass during the previous particle calculation.
4. Recalculate the particle trajectories, temperature, and mass based on the updated gas-phase flow field.

5. Repeat the last two steps until a converged solution is achieved, in which both the gas-phase flow field and the particle trajectories are unchanged comparing two successive calculations.

In the coupled calculation, the particle-phase iteration is performed at specified time intervals during the gas-phase calculation. To ensure the good convergence of the numerical solutions, the frequency of the interaction between gas phase and discrete phase is specified as 20 iterations of gas phase per DPM iteration. For each discrete-phase iteration, the particle trajectories, temperature, and mass are computed and the interphase exchange of momentum, heat, and mass is updated in each control volume. These interphase exchange terms then impact the gas phase when the gas phase iteration is performed. The coupled calculation continues until the gas-phase flow field no longer changes with further calculations.

The trajectory equation and the auxiliary equations describing heat or mass transfer to/from the particle are solved by stepwise integration over discrete time steps. The differential Eq. 6 is solved using a trapezoidal discretization scheme. The new particle location is also computed by the same scheme. The time step size used to integrate the equation of motion for the particle within each control volume is determined by the estimated transit time and the step length factor, as $\Delta t = \Delta t^*/\chi$, where Δt^* is the time required for the particle to traverse the current continuous phase control volume, which is estimated using the current particle velocity; χ is the step length factor, which is set to 50 to make sure a good convergence. In this study, the time step is also used to integrate the auxiliary equations describing heat or mass transfer to/from the particle by assuming that the temperature and mass of the particle do not change significantly between time steps ($\sim$1 μs). Therefore, the differential Eq. 11 is discretized with second-order discretization in space and first-order discretization in time. The particle is divided into 45 shells equally spaced along the radial direction in this study. Thus, the good convergence could be ensured for the numerical solutions.

The solution of the particle motion, heat, and mass equations are solved in a segregated manner. During each time step, the new particle location and particle velocity are computed first according to the particle velocity and fluid velocity at the old location. As the particle trajectory is computed, Eq. 11 is integrated to obtain the temperature distribution inside particle based on the physical property parameters and boundary conditions got from the old particle location. Once the temperature distribution is obtained, the particle devolatilization behavior (mass loss) can be calculated using the improved CPD model.

Manuscript received May 19, 2012, and revision received Sept. 28, 2012.